

Surface control and MBE growth diagram for homoepitaxy on single-crystal AlN substrates

Cite as: Appl. Phys. Lett. **116**, 262102 (2020); doi: [10.1063/5.0010813](https://doi.org/10.1063/5.0010813)

Submitted: 15 April 2020 · Accepted: 17 June 2020 ·

Published Online: 30 June 2020









View Online



Export Citation



CrossMark

Kevin Lee,^{1,a)}  YongJin Cho,¹  Leo J. Schowalter,²  Masato Toita,²  Huili Grace Xing,^{1,3,4} 
and Debdeep Jena^{1,3,4} 

AFFILIATIONS

¹School of Electrical and Computer Engineering, Cornell University, Ithaca, New York 14853, USA

²Advanced Devices Technology Center, Asahi Kasei Corporation, Hibiya Mitsui Tower, 1-1-2 Yurakucho, Chiyoda-ku, Tokyo 100-8440, Japan

³Department of Materials Science and Engineering, Cornell University, Ithaca, New York 14853, USA

⁴Kavli Institute for Nanoscale Science, Cornell University, Ithaca, New York 14853, USA

^{a)}Author to whom correspondence should be addressed: kl833@cornell.edu

ABSTRACT

The evolution of surface morphology for single-crystal bulk Al-polar aluminum nitride substrates during *ex situ* cleaning, *in situ* cleaning, and subsequent homoepitaxy is investigated. *Ex situ* acid treatment is found to reveal atomic steps on the bulk AlN substrates. After *in situ* Al-assisted cleaning at high temperatures in a high vacuum environment monitored with reflection high-energy electron diffraction, cleaner atomic step edges are observed. Subsequent growth on the cleaned bulk AlN by molecular beam epitaxy is used to develop a phase-diagram for homoepitaxy on AlN single crystals. Secondary ion mass spectrometry profiles reveal high-purity epitaxial layers with undesired chemical impurity densities of Si, O, and C to be below detection limits. The grown homoepitaxial films are observed to oxidize in the ambient environment, but repeating the *ex situ* acid treatment again reveals atomic steps.

Published under license by AIP Publishing. <https://doi.org/10.1063/5.0010813>

Wurtzite AlN possesses a wide direct energy bandgap of 6.1 eV, a high thermal conductivity, a high breakdown voltage, and a large piezoelectric constant. These properties make it an ideal choice for UV photonic devices, power electronics, and bulk acoustic wave filters.^{1–5} Because AlN is traditionally grown by heteroepitaxy on lattice-mismatched silicon, SiC or sapphire substrates by metal-organic chemical vapor deposition (MOCVD), hydride vapor phase epitaxy (HVPE), or molecular beam epitaxy (MBE),^{6–10} the resulting films have high dislocation densities. This contributes to high leakage currents in AlN-based high electron mobility transistors (HEMTs) and low internal quantum efficiencies in UV-LEDs.^{11–13} High-quality single-crystal bulk AlN is therefore desired to mitigate these problems. Recently, Al-polar bulk AlN single-crystals grown by physical vapor transport (PVT) have become available.^{14–17} These substrates exhibit dislocation densities $< 10^4 \text{ cm}^{-2}$ and were instrumental in the demonstration of the first electrically pumped UV-C laser.¹⁸

The first challenge for homoepitaxy on bulk AlN substrates is obtaining an atomically and chemically clean surface. The surface of Al-polar AlN is known to spontaneously form oxides (Al_2O_3) and hydroxides (AlOOH and $\text{Al}(\text{OH})_3$).^{19–22} Using X-ray photoelectron

spectroscopy (XPS) and Auger electron spectroscopy (AES), King *et al.* have studied the efficacy of *ex situ* wet chemical treatments (HCl, HF, KOH, H_3PO_4 , H_2SO_4 , and Piranha) and *in situ* annealing in cleaning the AlN surface.²³ They found that buffered HF removes surface oxides but leaves a small amount of fluorine on the surface, which requires *in situ* annealing at 950 °C to remove completely. However, complete removal of oxygen is not possible even at annealing temperatures > 1100 °C after the HF treatment.

The incomplete removal of oxides and hydroxides hinders the effective nucleation on AlN single-crystal substrates and promotes undesired chemical and structural defects. Rice *et al.* reported that treating the AlN surface with a mixture of sulfuric and phosphoric acids heated to 90 °C for 10 min removes hydroxide contaminants.²⁴ Afterward, they performed a high temperature (1250 °C) ammonia anneal in an MOCVD chamber to convert the surface hydroxide into AlN. AlN homoepitaxy was then performed on the annealed surface, after which atomic steps were observed.

Using plasma-assisted MBE, Nakajima *et al.* observed that hydroxide and oxide residues on the SiC surface increase the pit density in subsequent heteroepitaxial AlN films.²⁵ Reports on the

nucleation and homoepitaxial growth of AlN on bulk AlN substrates by MBE, however, are rare. Recently, Cho *et al.* developed an Al-assisted *in situ* surface cleaning method, which enables AlN homoepitaxy on bulk AlN.²⁶ Secondary ion mass spectrometry (SIMS) measurements showed that this method led to a drastically lower oxygen impurity concentration at the nucleation interface in comparison with performing a high temperature anneal without Al-assisted cleaning. Cross-sectional scanning transmission electron microscopy (STEM) imaging together with SIMS showed that Al-assisted cleaning at high temperatures in the MBE chamber enables true homoepitaxy free of chemical and structural defects, with parallel atomic steps present on the AlN surface. On the other hand, direct epitaxy on single-crystal bulk AlN without the *in situ* Al-assisted cleaning step exhibited rough surface morphologies along with structural and chemical defects.

In this report, we first investigate the effects of *ex situ* and *in situ* cleaning on the surface morphology of bulk Al-polar AlN, before performing any epitaxy. We find that *ex situ* acid treatment reveals atomic step edges. Subsequently, AlN homoepitaxy is performed by PA-MBE. Growth at high temperatures in Al-rich conditions is found to produce parallel atomic steps. At low growth temperatures, a mix of 2D steps and 3D islands is observed due to limited adatom diffusion. This study helps identify a growth phase diagram for homoepitaxy on single-crystal bulk AlN substrates. SIMS analysis of the high-quality homoepitaxial AlN films indicates low chemical impurity densities near the detection limit. Finally, the subsequent surface oxidation of the films after exposure to the ambient environment and acid cleaning to reveal atomic steps are observed by AFM.

The bulk substrates used in this study are 2-in. diameter Al-polar AlN substrates from crystal IS with dislocation densities of $\sim 10^4 \text{ cm}^{-2}$. The wafers were diced into $1 \times 1 \text{ cm}^2$ pieces for cleaning and growth. A flow chart summary of the cleaning process is presented in Fig. 1(a), along with the AFM images taken during the process [Figs. 1(b)–1(d)]. Figure 1(b) shows a representative surface after the *ex situ* solvent cleaning (consisting of 10 min of sonication in acetone and 5 min in 2-propanol). The surface was smooth with sub-nm roughness, but no atomic steps were observed. The substrates were then cleaned in 1:3 $\text{H}_3\text{PO}_4:\text{H}_2\text{SO}_4$ heated at 70°C for 5 min, followed by a 5-min de-ionized water rinse. Next, the substrates were treated with 10% HF for 15 min, followed by another 5-min de-ionized water rinse, concluding the *ex situ* cleaning. These treatments revealed atomic steps as shown in Fig. 1(c), with a surface roughness of 1.3 Å inside atomic step terraces shown by the blue boxed regions, including jagged edges and some debris. Because the surface root-mean square (rms) roughness can be overestimated due to the atomic step terraces in the image, a $150 \times 150 \text{ nm}^2$ box inside the atomic step terraces is chosen instead of the entire area for the rms evaluation of the AFM data. This method eliminates artificial roughness resulting from atomic steps. Using Piranha solution instead of 1:3 $\text{H}_3\text{PO}_4:\text{H}_2\text{SO}_4$ revealed similar atomic steps. The jagged edges likely stem from the incomplete removal of surface oxides and hydroxides, as the chemical reaction in ambient air likely originates at the step edges. The substrates were then mounted on a faceplate with a front holder plate and a molybdenum heat diffuser plate on the back, after which they were transferred into the load-lock chamber of a PA-MBE Veeco GEN10 plasma-MBE system and baked at 200°C for 8 h.

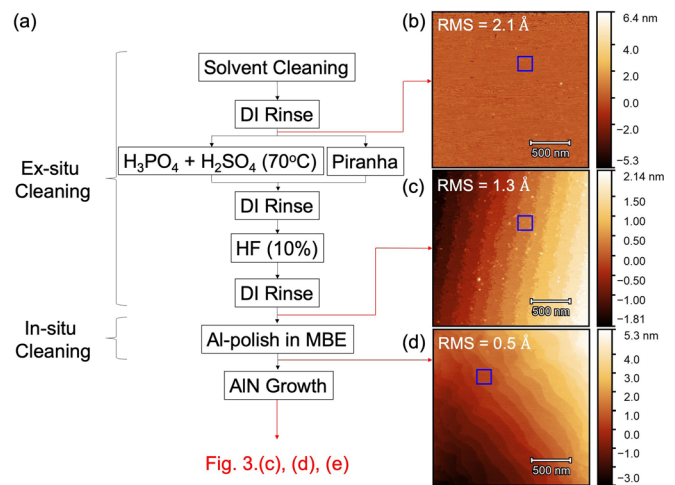


FIG. 1. (a) Cleaning process flow chart before epitaxy for single-crystal AlN. AFM images of the bulk AlN surface after (b) solvent cleaning, (c) cleaning in $\text{H}_3\text{PO}_4:\text{H}_2\text{SO}_4$ (1:3) at 70°C for 5 min and 10% HF for 15 min, and (d) Al-assisted surface cleaning inside the MBE system. Root-mean square (RMS) roughness calculated over the blue box region of $150 \times 150 \text{ nm}^2$ for each image is indicated above the images.

In situ chemical cleaning of the substrates was then performed in the MBE growth chamber at a background pressure of $\sim 10^{-9}$ Torr without a flowing nitrogen gas. The substrates were heated up to a thermocouple temperature of 1150°C and then exposed to an aluminum metal flux of 9.13 nm/min for 30 s. The high temperature was held long enough for the deposited Al to desorb. This process of adsorption and desorption, which we call Al-polishing, was clearly resolved using reflection high-energy electron diffraction (RHEED), as shown in Fig. 2. Figure 2(a) tracks the intensity vs time of the boxed area in Fig. 2(b). The intensity is found to drop when Al is deposited and increase when it desorbs.²⁷ This process was repeated for several cycles. The third through fifth cycles were observed to be qualitatively distinct from the first and second. The reason for such a difference in behavior is tied to the presence of oxides on the surface. During the first two cycles, Al metal reacts with the surface oxide producing a volatile suboxide ($\text{Al}_2\text{O}_3 + 4\text{Al} \rightarrow 3\text{Al}_2\text{O} \uparrow$), which decomposes at the high substrate temperature.²⁸ After these cycles, surface oxide is completely removed, so the adsorption and desorption for subsequent cycles follow a different two-step process, as shown in red in Fig. 2(c), similar to the Ga bilayer and droplet formation on Ga-polar GaN surfaces.^{29–32} This change in behavior provides an accurate marker when the surface becomes free of contamination. After this *in situ* Al-polishing, a substrate was rapidly transferred (to minimize air-exposure) to the AFM chamber for imaging. In place of the previous jagged edges, clean atomic step edges were observed, as shown in Fig. 1(d). The surface is free of debris with a roughness of 0.5 \AA . A similar cleaning process at a slightly lower thermocouple temperature of 1120°C is also effective, but the first desorption process takes much longer time.

After the *ex situ* and *in situ* cleaning, AlN homoepitaxy was performed directly. Due to differences in mounting techniques or system design, the measured thermocouple temperatures can differ from the actual surface temperatures of the crystal and vary from system to system. The desorption of Al metal on the AlN surface, however, is a

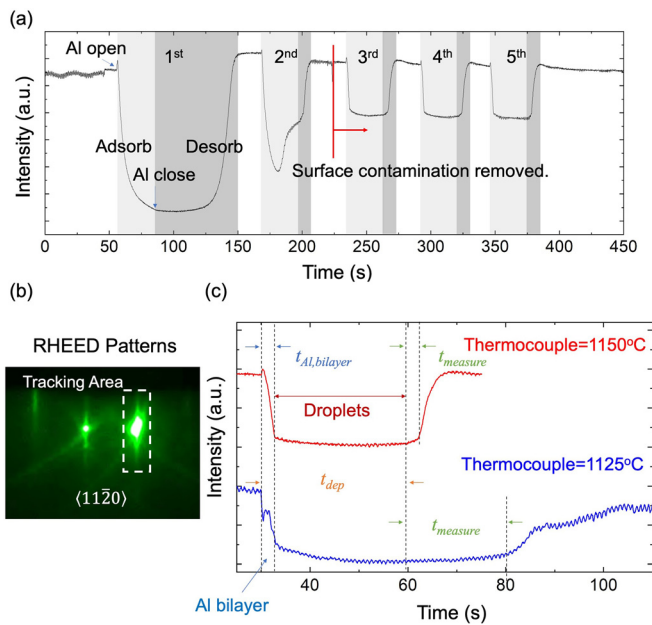


FIG. 2. (a) RHEED intensity vs time, tracking five cycles of Al-assisted cleaning. The light gray shaded area corresponds to Al deposition on the surface, while the dark gray shaded area corresponds to the desorption process. (b) RHEED image showing the diffraction pattern along $(11\bar{2}0)$, with the electron beam voltage and current at 14.5 kV and 1.45 A, respectively. The white box marks the area in which the intensity is tracked. (c) Red curve: zoomed-in image of the third cycle in (a) with thermocouple temperature at 1150 °C, while the blue curve shows the desorption process under a lower thermocouple temperature at 1125 °C. The regions corresponding to chemical adsorption (Al bilayer), physical adsorption (droplet formation), and total Al deposition time are denoted by blue, red, and orange arrows, respectively. Green arrows indicate the time required for Al droplet desorption.

physical process, and its dependence on the surface thermal condition is universal. Thus, the Al droplet desorption rate is a more accurate description of the surface thermal condition. We first evaluate the desorption rate of Al droplets on the crystal surface from the RHEED intensity, as shown in Fig. 2(c), at several substrate temperatures. The Al droplet desorption rate Φ_{des} on the AlN surface is determined as $\Phi_{des} = (\Phi_{Al})(t_{dep} - t_{Al,bilayer}) / (t_{dep} - t_{Al,bilayer} + t_{measure})$, where Φ_{Al} is the Al metal flux, t_{dep} is the Al deposition time, $t_{measure}$ is the Al droplet desorption time, and $t_{Al,bilayer}$ is the Al bilayer formation time. Figure 3(a) shows a set of experimental Al droplet desorption rate data vs different thermocouple temperatures. The Al desorption rate exhibits Arrhenius behavior with an activation energy of 3.81 eV, as shown in the inset of Fig. 3(a), similar to the report by Koblmüller *et al.*³³ The Al desorption rate is important since it represents the boundary between Al-rich and intermediate growth regions, as shown in Fig. 3(b).

High-performance electronic and photonic devices such as HEMTs, UV-LEDs, and lasers require alloys and heterostructures of AlN with GaN. To grow GaN or AlGaIn, lower growth temperatures are required to avoid Ga desorption. To that end, the surface morphologies of AlN at various growth temperatures were explored. The N_2 plasma power was held at 400 W with 2 sccm flow rate, corresponding to a growth rate of 7.5 nm/min. Al metal was provided through a standard effusion cell. AlN films of thicknesses between 220 and 360 nm

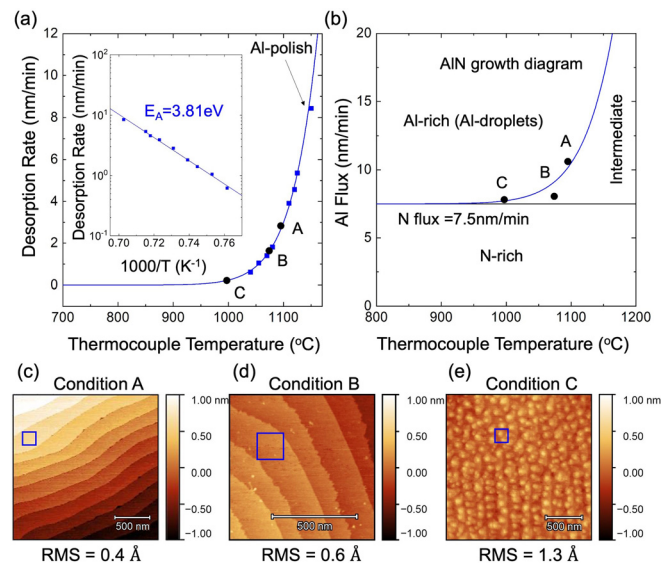


FIG. 3. (a) Desorption rate of Al droplets on the Al-polar AlN surface. Blue dots are representative experimental data on crystal IS bulk AlN substrates mounted by a faceplate. The inset figure is an Arrhenius plot of the experimental data. The fitted line shows an activation energy of 3.81 eV. Black dots represent the desorption rates of conditions A, B, and C. (b) AlN growth diagram for homoepitaxy. (c) $2 \times 2 \mu\text{m}^2$ AFM image of AlN grown at 1095 °C with an atomic step height of 2.44 Å. (d) $1 \times 1 \mu\text{m}^2$ AFM image of condition B, showing the smooth regions between pits; pits (not shown) are observed on the epi-surface due to the low Al/N ratio. (e) $2 \times 2 \mu\text{m}^2$ AFM image of condition C with 2D steps and 3D islands.

were grown. Figure 3(b) shows the MBE growth diagram for the homoepitaxy of AlN. Al-rich (III/V ratio > 1) conditions are preferred for two-dimensional growth.³³ The epitaxial process was started by first opening the Al shutter for 20 s to wet the surface. Then, both Al and nitrogen shutters were left open for the entire duration of AlN growth. To end the growth, the plasma is turned off, both Al and N_2 shutters are closed, and the substrate is heated to 50 °C higher than the growth temperature to desorb excess Al. The highest investigated growth temperature was condition A at 1095 °C, which corresponded to a desorption rate $\Phi_{des} = 2.83$ nm/min. Figure 3(c) shows that this growth condition results in smooth parallel atomic steps with average step heights and widths of 2.44 Å (~ 1 monolayer of AlN) and 200 nm, respectively. Condition B at a lower temperature of 1074 °C ($\Phi_{des} = 1.64$ nm/min) and in the intermediate III/V ratio regime also results in 2D growth, but because of the insufficient Al surface coverage, pits are generated. Figure 3(d) shows that the surface morphology between pits for a smaller scan area of $1 \times 1 \mu\text{m}^2$ still has atomic steps. Finally, the lowest growth temperature of 997 °C ($\Phi_{des} = 0.22$ nm/min) in condition C yields the surface morphology shown in Fig. 3(e). A combination of both parallel atomic steps and 3D islands is observed, albeit with a smooth surface with an rms roughness of ~ 1.3 Å for a $150 \times 150 \text{ nm}^2$ scan area. The mechanisms for the evolution of such morphology have been proposed in recent MOCVD reports.³⁴ The low growth temperature reduces the surface diffusion length of Al adatoms, promoting nucleation at the center of the atomic steps, where the highest supersaturation occurs, resulting in 3D islands. The Al adatoms are able to diffuse to the step edges at higher

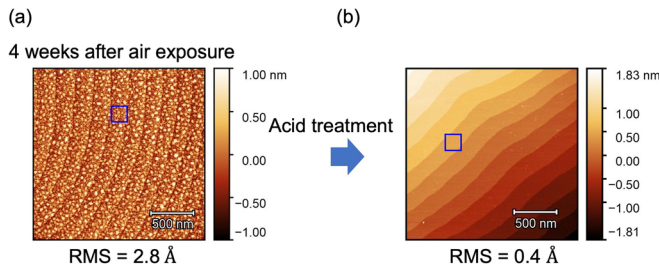


FIG. 4. (a) AFM image corresponding to the sample surface under condition A after exposure to air for 4 weeks. (b) AFM image of the same sample (exposed to air for 4 weeks) after acid treatment.

growth temperatures, enabling homoepitaxial growth by MBE with parallel atomic steps.

The effects of long exposure to ambient conditions on the epitaxial surfaces were investigated. The sample grown in condition A was exposed to air for 4 weeks. Small particles were observed on the surface as shown in Fig. 4(a), which could be completely removed to again reveal the atomic steps as shown in Fig. 4(b) by treating the surface with $\text{H}_3\text{PO}_4\text{:H}_2\text{SO}_4$ in the same manner as mentioned earlier in the *ex situ* cleaning description. The incorporation of chemical impurities in the homoepitaxially grown AlN was studied by SIMS (performed by the Evans Analytical Group) on a sample with $\sim 1\ \mu\text{m}$ of AlN grown at 1107°C ($\Phi_{\text{des}} = 3.66\ \text{nm}/\text{min}$) under Al-rich conditions similar to condition A. Figure 5 shows that the impurity concentrations for Si, O, H, and C are all very near or below the detection limit throughout the $1\ \mu\text{m}$ epitaxial AlN layer away from the nucleation interface (the detection limits are 1×10^{17} atoms/ cm^3 for Si and O, $1\text{--}2 \times 10^{17}$ atoms/ cm^3 for H, and $4\text{--}5 \times 10^{16}$ atoms/ cm^3 for C). Peaks for C and much smaller peaks for O and Si were observed at the nucleation interface with concentrations of $\sim 4.2 \times 10^{19}$ atoms/ cm^3 , $\sim 1.1 \times 10^{18}$ atoms/ cm^3 , and $\sim 1.5 \times 10^{18}$ atoms/ cm^3 , respectively. These peaks

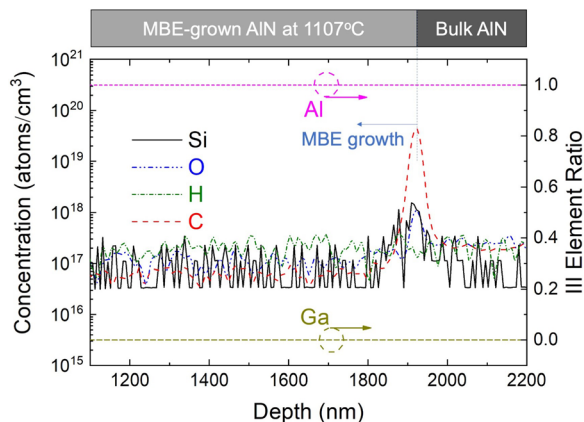


FIG. 5. Secondary ion mass spectrometry profile of silicon, oxygen, hydrogen, and carbon in the AlN epitaxial films grown by PA-MBE. The peak concentrations for C, O, and Si at the growth interface are $\sim 4.2 \times 10^{19}$ atoms/ cm^3 , $\sim 1.1 \times 10^{18}$ atoms/ cm^3 , and $\sim 1.5 \times 10^{18}$ atoms/ cm^3 , respectively. The III element ratio is specified on the right axis. The Ga content is less than 1% throughout the film, suggesting that there is no Ga contamination in the AlN.

decayed to background levels within 100 nm of the epitaxial layer. The *in situ* Al-polishing has been found to be effective in significantly reducing the concentration of Si and O at the AlN homoepitaxy growth interface.²⁶ However, the carbon concentration is comparable to that in the homoepitaxial sample without *in situ* Al polishing. We speculate that the carbon is present on the AlN substrate surface prior to loading into the MBE system and cannot be removed with Al-polishing. It is worth noting that carbon can be nearly all removed using thermal annealing at $\sim 1450^\circ\text{C}$.²⁶ In any case, the C impurity concentration in the MBE-grown AlN epitaxial layer was found to be very close to the detection limit of $4\text{--}5 \times 10^{16}$ atoms/ cm^3 . Dalmou *et al.* have reported C levels around 1×10^{18} atoms/ cm^3 in MOCVD growth,³⁵ presumably due to the C from the metal-organic precursors, which is absent in the MBE environment. Minimizing carbon is particularly important for UV photonic devices because C impurities in bulk AlN substrates have been found to absorb at 265 nm.³⁶ The low C impurity concentration observed here in the homoepitaxial AlN layers grown by MBE is, thus, of interest for UV-LEDs and lasers.

In conclusion, it is found that clean atomic steps are revealed on single-crystal bulk AlN substrates through *ex situ* surface acid cleaning followed by *in situ* Al-polishing in MBE. The *ex situ* cleaning alone results in atomic steps with jagged edges, which are converted to clean edges by the *in situ* Al-polishing. AlN homoepitaxy on cleaned AlN bulk substrates at a high growth temperature of 1095°C results in parallel smooth atomic steps, but at 997°C , it results in 3D islands. A growth diagram of AlN by MBE was developed, resulting in the identification of a growth condition that yields smooth surface morphologies and true homoepitaxy, with impurity concentrations near the detection limits throughout the epitaxial layers. The surface control and growth diagram developed here qualify MBE as a promising method for the growth of high-performance electronic and photonic devices on bulk AlN substrates in the future.

The authors at Cornell University acknowledge financial support from Crystal IS, the Cornell Center for Materials Research (CCMR)—an NSF MRSEC program (No. DMR-1719875), and an AFSOR Grant No. FA9550-17-1-0048. This work uses the CESI Shared Facilities partly sponsored by the NSF MRI No. DMR-1338010 and the Kavli Institute at Cornell (KIC).

DATA AVAILABILITY

The data that support the findings of this study are available from the corresponding author upon reasonable request.

REFERENCES

- Y. Taniyasu, M. Kasu, and T. Makimoto, *Nature* **441**, 325 (2006).
- S. M. Islam, K. Lee, J. Verma, V. Protasenko, S. Rouvimov, S. Bharadwaj, H. Xing, and D. Jena, *Appl. Phys. Lett.* **110**, 041108 (2017).
- X. H. Li, T. Detchprohm, T. T. Kao, M. M. Satter, S. C. Shen, P. Douglas Yoder, R. D. Dupuis, S. Wang, Y. O. Wei, H. Xie, A. M. Fischer, F. A. Ponce, T. Wernicke, C. Reich, M. Martens, and M. Kneissl, *Appl. Phys. Lett.* **105**, 141106 (2014).
- A. Hickman, R. Chaudhuri, S. J. Bader, K. Nomoto, K. Lee, H. G. Xing, and D. Jena, *IEEE Electron Device Lett.* **40**, 1293 (2019).
- S. Mahon and R. Aigner, in *International Conference Compound Semiconductor Manufacturing Technology (CS MANTECH 2007)* (2007), p. 15.
- M. Imura, K. Nakano, N. Fujimoto, N. Okada, K. Balakrishnan, M. Iwaya, S. Kamiyama, H. Amano, I. Akasaki, T. Noro, T. Takagi, and A. Bandoh, *Jpn. J. Appl. Phys., Part 1* **45**, 8639 (2006).

- ⁷T. Baker, A. Mayo, Z. Veisi, P. Lu, and J. Schmitt, *Phys. Status Solidi C* **11**, 373 (2014).
- ⁸N. Teraguchi, A. Suzuki, Y. Saito, T. Yamaguchi, T. Araki, and Y. Nanishi, *J. Cryst. Growth* **230**, 392 (2001).
- ⁹V. N. Jmerik, A. M. Mizerov, D. V. Nechaev, P. A. Aseev, A. A. Sitnikova, S. I. Troshkov, P. S. Kop'Ev, and S. V. Ivanov, *J. Cryst. Growth* **354**, 188 (2012).
- ¹⁰N. Onojima, J. Suda, and H. Matsunami, *Appl. Phys. Lett.* **80**, 76 (2002).
- ¹¹Y. Yamaoka, A. Ubukata, Y. Yano, T. Tabuchi, K. Matsumoto, and T. Egawa, *Semicond. Sci. Technol.* **34**, 035015 (2019).
- ¹²M. Kneissl, T. Kolbe, C. Chua, V. Kueller, N. Lobo, J. Stellmach, A. Knauer, H. Rodriguez, S. Einfeldt, Z. Yang, N. M. Johnson, and M. Weyers, *Semicond. Sci. Technol.* **26**, 014036 (2011).
- ¹³K. Ban, J. I. Yamamoto, K. Takeda, K. Ide, M. Iwaya, T. Takeuchi, S. Kamiyama, I. Akasaki, and H. Amano, *Appl. Phys. Express* **4**, 052101 (2011).
- ¹⁴P. Lu, R. Collazo, R. F. Dalmau, G. Durkaya, N. Dietz, B. Raghathamachar, M. Dudley, and Z. Sitar, *J. Cryst. Growth* **312**, 58 (2009).
- ¹⁵M. Bickermann, B. M. Epelbaum, O. Filip, P. Heimann, S. Nagata, and A. Winnacker, *Phys. Status Solidi C* **7**, 21 (2010).
- ¹⁶Y. Kumagai, Y. Kubota, T. Nagashima, T. Kinoshita, R. Dalmau, R. Schlessler, B. Moody, J. Xie, H. Murakami, A. Koukitu, and Z. Sitar, *Appl. Phys. Express* **5**, 055504 (2012).
- ¹⁷R. T. Bondokov, S. G. Mueller, K. E. Morgan, G. A. Slack, S. Schujman, M. C. Wood, J. A. Smart, and L. J. Schowalter, *J. Cryst. Growth* **310**, 4020 (2008).
- ¹⁸Z. Zhang, M. Kushimoto, T. Sakai, N. Sugiyama, L. J. Schowalter, C. Sasaoka, and H. Amano, *Appl. Phys. Express* **12**, 124003 (2019).
- ¹⁹L. M. Svedberg, K. C. Arndt, and M. J. Cima, *J. Am. Ceram. Soc.* **83**, 41 (2000).
- ²⁰R. Korbutowicz, A. Zakrzewski, O. Rac-Rumijowska, A. Stafniak, and A. Vincze, *J. Mater. Sci. Mater. Electron.* **28**, 13937 (2017).
- ²¹P. Bowen, J. G. Highfield, A. Mocellin, and T. A. Ring, *J. Am. Ceram. Soc.* **73**, 724 (1990).
- ²²Y. Chen, X. Hou, Z. Fang, E. Wang, J. Chen, and G. Bei, *J. Phys. Chem. C* **123**, 5460 (2019).
- ²³S. W. King, J. P. Barnak, M. D. Bremser, K. M. Tracy, C. Ronning, R. F. Davis, and R. J. Nemanich, *J. Appl. Phys.* **84**, 5248 (1998).
- ²⁴A. Rice, R. Collazo, J. Tweedie, R. Dalmau, S. Mita, J. Xie, and Z. Sitar, *J. Appl. Phys.* **108**, 043510 (2010).
- ²⁵A. Nakajima, Y. Furukawa, S. Koga, and H. Yonezu, *J. Cryst. Growth* **265**, 351 (2004).
- ²⁶Y. Cho, C. S. Chang, K. Lee, M. Gong, K. Nomoto, M. Toita, L. J. Schowalter, D. A. Muller, D. Jena, and H. G. Xing, *Appl. Phys. Lett.* **116**, 172106 (2020).
- ²⁷S. Tamariz, D. Martin, and N. Grandjean, *J. Cryst. Growth* **476**, 58 (2017).
- ²⁸C. N. Cochran, *J. Am. Chem. Soc.* **77**, 2190 (1955).
- ²⁹J. E. Northrup and J. Neugebauer, *Phys. Rev. B* **61**, 9932 (2000).
- ³⁰C. D. Lee, Y. Dong, R. M. Feenstra, J. E. Northrup, and J. Neugebauer, *Phys. Rev. B* **68**, 205317 (2003).
- ³¹Y. Kangawa, T. Akiyama, T. Ito, K. Shiraishi, and T. Nakayama, *Material* **6**, 3309 (2013).
- ³²P. Misra, C. Boney, D. Starikov, and A. Bensaoula, *J. Cryst. Growth* **311**, 2033 (2009).
- ³³G. Koblmüller, R. Averbeck, L. Geelhaar, H. Riechert, W. Höslner, and P. Pongratz, *J. Appl. Phys.* **93**, 9591 (2003).
- ³⁴I. Bryan, Z. Bryan, S. Mita, A. Rice, J. Tweedie, R. Collazo, and Z. Sitar, *J. Cryst. Growth* **438**, 81 (2016).
- ³⁵R. Dalmau, B. Moody, R. Schlessler, S. Mita, J. Xie, M. Feneberg, B. Neuschl, K. Thonke, R. Collazo, A. Rice, J. Tweedie, and Z. Sitar, *J. Electrochem. Soc.* **158**, H530 (2011).
- ³⁶R. Collazo, J. Xie, B. E. Gaddy, Z. Bryan, R. Kirste, M. Hoffmann, R. Dalmau, B. Moody, Y. Kumagai, T. Nagashima, Y. Kubota, T. Kinoshita, A. Koukitu, D. L. Irving, and Z. Sitar, *Appl. Phys. Lett.* **100**, 191914 (2012).